The International Journal of Advanced Manufacturing Technology (2024) 132:1151–1162
https://doi.org/10.1007/s00170-024-13314-3

ORIGINAL ARTICLE

Optimization of a tetrahedron compliant spherical joint via computer-aided engineering tools

Seyyed Masoud Kargar[1] · Alberto Parmiggiani[2] · Mario Baggetta[1] · Emilio Ottonello[2,3] · Guangbo Hao[4] · Giovanni Berselli[1,5]

Received: 10 September 2023 / Accepted: 16 February 2024 / Published online: 19 March 2024

Abstract
This article focuses on enhancing the range of motion (ROM) of the Tetra II joint, a spherical compliant joint consisting of three internally interconnected tetrahedron-shaped elements that achieve motion through elastic deformation. Despite its excellent precision, this specific design is constrained in terms of ROM due to internal contacts among the tetrahedral elements. To overcome this limitation, this study utilizes a computer-aided engineering (CAE) framework to optimize the configuration of the Tetra II joint and enhance its ROM. The resultant optimized joint, referred to as Tetra III, is subsequently compared to Tetra II in terms of both ROM and center shift. Finite element models (FEM) are employed to validate the optimization results and examine how various tetrahedron-shaped geometries impact the joint's performance. The newly optimized joint exhibits a significantly higher ROM compared to the previous version, while maintaining excellent precision and overall smaller dimensions. Finally, to demonstrate its manufacturability, the Tetra III joint is produced using selective laser sintering (SLS) technology, with Duraform PA serving as the construction material. The successful fabrication serves as a demonstrative example of the improved design of the Tetra III joint.

Keywords Compliant mechanisms · Tetrahedron · Flexure · Spherical joint · CAE · PRBM · SLS

1 Introduction

Compliant mechanisms set themselves apart from rigid-body mechanisms by deriving their motion and force transmission from the deflection of flexible members. Unlike conventional rigid-body joints, compliant joints achieve motion through elastic deformation, providing benefits such as frictionless displacement and the absence of backlash. Additionally, compliant joints necessitate fewer components for operation and can be designed to be more compact. The absence of contact between rigid surfaces also reduces wear and the need for lubrication, contributing to improved mechanism precision. Furthermore, advancements in materials and production technologies, such as additive manufacturing, along with emerging fields of application like miniaturized assembly, have spurred increased research and exploration in the realm of compliant mechanisms. These distinctive characteristics, coupled with ongoing progress in this field, underscore the potential of compliant mechanisms to enhance performance and facilitate innovative solutions across various domains [1, 2].

A ball and socket joint, also known as a spherical joint, is a type of mechanical joint that facilitates a broad range of rotational motion across multiple axes. It enables movement around three perpendicular axes, resembling the movement of a ball within a socket. This type of joint is commonly found in various mechanical systems [3], including the human body [4]. Spherical compliant joints offer a high-precision alternative to traditional ball and socket joints by utilizing the deflection of slender segments to achieve motion, thereby obtaining all the intrinsic advantages of compliant mechanisms previously listed [5–7].

Spherical compliant joints are commonly found in flexure-based precision spatial manipulators that employ parallel kinematic arrangements. Examples of such applications include compliant conventional parallel kinematic machines [8], nanopositioners [9], and compliant parallel mechanisms [10, 11]. In these applications, spherical motion is achieved using either spherical notch joints or short wire flexures. The notch joint offers compact and streamlined designs,

✉ Giovanni Berselli
giovanni.berselli@unige.it

Extended author information available on the last page of the article

facilitating easy manufacturing. However, its range of motion (ROM) is limited, typically confined to a few degrees. To enable larger rotation angles, an alternative approach involves constructing spherical joints using stacked arrangements of wire flexures [12]. While this approach allows for a wider ROM, it comes with a decrease in support stiffness as the deflection angle increases. Moreover, the long and slender geometry of these joints makes them susceptible to buckling, imposing limitations on their load-bearing capacity [13]. In addition to these arrangements, the literature introduces alternative designs of spherical compliant joints capable of enabling three rotations at a single point. The development of these innovative joint designs exemplifies the potential of compliant mechanisms to enhance the precision and functionality across a wide range of applications [5]. Lobontiu and Paine [14] introduced a circular cross-section corner-filleted flexure hinge to enable three-dimensional compliant mechanisms. The use of a thin circular cross-section facilitates three rotations while limiting translations. To impose constraints on each translation, a wire flexure was integrated to the end-effector at [12, 15]. Notably, these three wire flexures intersect at a shared point in space, enhancing the mechanical characteristics of the design. Building on the concept of rigid spherical linkage, a spherical joint was devised where the axes of three revolute joints converge at a single point [10, 16]. Naves et al. [13] employed three folded leaf springs to create spherical flexure joints. Each leaf spring effectively constrains one translational motion and allows rotation in space. Lastly, Rommers et al. [5] developed the Tetra II joint by serially connecting tetrahedron-shaped elements without intermediate bodies. We find the Tetra II joint especially suitable for compliant robots due to its compact design and self-supporting structure, making it particularly well-suited for additive manufacturing. In our earlier research, we presented a monolithic delta robot [17] (Fig. 1) incorporating compliant spherical joints. The parallel robot architecture has demonstrated remarkable versatility and adaptability, as evidenced by its continued application in diverse fields [18–20]. Notably, the recent progress in additive manufacturing has facilitated the integration of compliant mechanisms, leveraging enhanced design flexibility and cost-effectiveness, as exemplified by previous studies [5, 21].

These joints are optimized, as presented in this paper, building upon the Tetra II joint (Fig. 2 (a) [5, 22]).

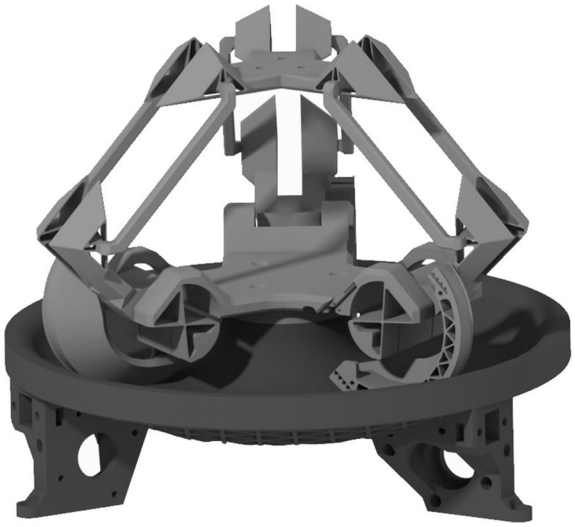

Fig. 1 DELTAFLEX [17]

1.1 Tetra joint background principles

As shown in Fig. 2 (a), the Tetra II joint comprises internally interconnected tetrahedron-shaped elements, each incorporating blade flexures and connected directly without the need for intermediate components. The design draws inspiration from the infinity hinge [23, 24] and features tetrahedron elements arranged in a nested configuration. These tetrahedron elements are interconnected in a series arrangement. Within the Tetra II design, point P serves as the floating remote center of rotation, situated in space (Fig. 2 (b)). The blade flexures effectively constrain the end-effector, e, allowing unrestricted rotations solely around point P. As depicted in Fig. 2 (c), when a horizontal force is exerted at the end-effector (point e), the joint undergoes rotation around point P. This action results in the attainment of a spherical motion centered around point P. It is worth noting that the planes of all three blade flexures composing the tetrahedron elements must converge precisely at point P.

This work aims to enhance the previous research by addressing the issue of progressive joint stiffening resulting from self-collisions, which limits Tetra joint's applicability in specific use cases, such as monolithic delta robots. To illustrate this phenomenon, it is useful to consider a one-dimensional case as represented in Fig. 2 (d). In the Tetra II design, as the flexures are gradually deflected, the external, larger and most compliant tetrahedral elements reach their maximum deformation. This condition is equivalent to the case of a spring reaching its maximum compression length. Once this situation is reached, further deformations are obtained only with the remaining internal elements which are not yet fully compressed. This, however, produces an increasing stiffening of the joint as these elements come into contact with each other, thus complicating the achievement of large deformations.

We thus propose a modification to the design introduced by Rommers et al., shown in Fig. 2 (e). This modification aims to avoid joint stiffening caused by self-collisions by minimizing the number of inner tetrahedral components, thereby enhancing joint mobility. The primary challenge is to preserve the favorable kinematic properties of the Tetra II joint,

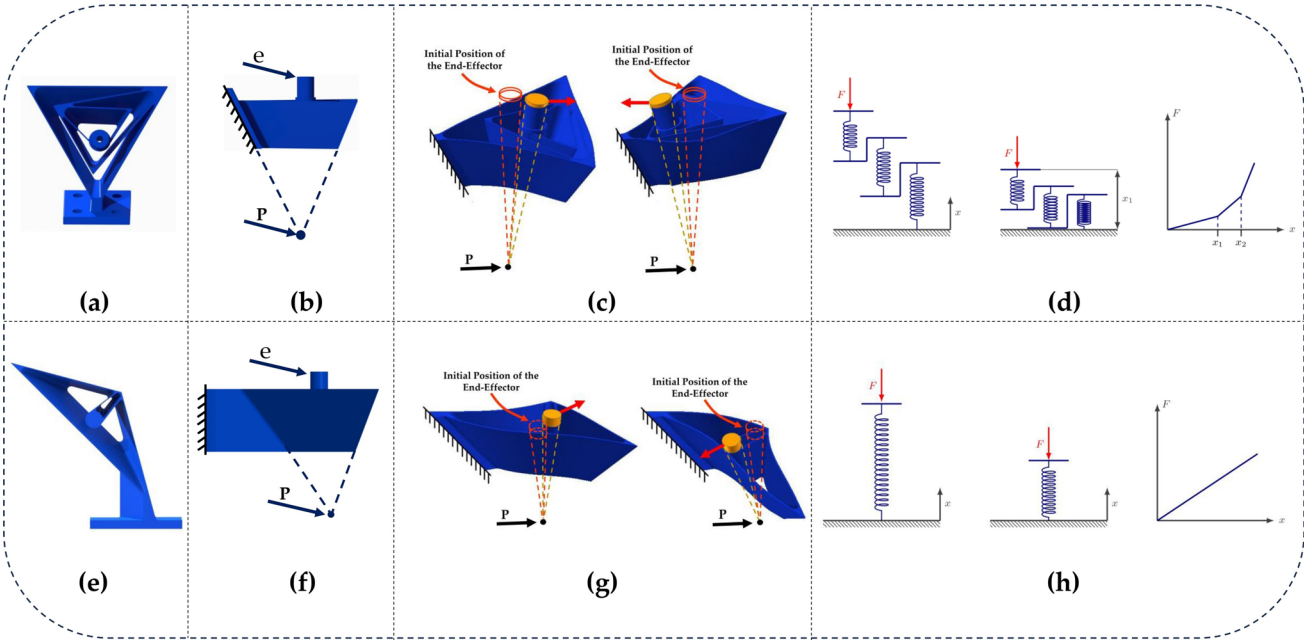

Fig. 2 (a) Tetra II [5]; (b) side view of Tetra II to show the end-effector and convergence of blade flexures in point P; and (c) deflected Tetra II. (d) 1D conceptual model of Tetra II. (e) Tetra III; (f) side view of Tetra III to show the end-effector and convergence of blade flexures in point P; and (g) deflected Tetra III. (h) 1D conceptual model of Tetra III

such as a constant center of rotation and resistance to parasitic motion, while simultaneously avoiding self-collisions.

In Tetra III, adopting the same design principles as Tetra II, point P serves as the floating remote center of rotation (Fig. 2 (f)). The blade flexures restrict the end-effector's movement, facilitating unrestricted rotations around point P. Unlike Tetra II, Tetra III achieves maximum mobility without the presence of inner components, As evident in Fig. 2 (g). Consequently, Tetra III overcomes the joint stiffening observed in Tetra II, as shown in Fig. 2 (h). The key benefits of Tetra III over Tetra II include significantly increased joint mobility due to the avoidance of self-collisions among inner components, thereby maximizing the overall ROM of the joint. This advantageous design characteristic is complemented by Tetra III's ability to maintain a lower center shift compared to Tetra II, a topic that will be thoroughly discussed in Section 3.

To achieve this, a computer-aided engineering (CAE) framework was employed to optimize spatial compliant mechanisms through Finite Element Analysis (FEA). The primary objective was to model and optimize the geometry of the Tetra II joint to enhance its ROM. To accomplish this, a parametric model was introduced and optimized using Spaceclaim scripting capabilities in conjunction with Ansys Workbench software. To enable faster simulations compared to FEM, a Pseudo-Rigid-Body equivalent model (PRBM) was developed and validated in a multi-body environment [1, 25, 26]. CAE-based frameworks have been demonstrated to be a versatile tool that has gained prominence in numerous applications [27]. Recent applications span a wide array of processes, including but not limited to weld joint analysis [28], injection molding [29–31], assessment of strain energy density [32], and advancements in casting processes [33]. Within the framework of our work, we employ CAE to optimize spatial compliant mechanisms, utilizing the effective pseudo-rigid body (PRB) modeling method [1, 25, 26].

Finally, the optimized Tetra joint, referred to as Tetra III, was designed and compared with Tetra II in terms of its ROM and center shift, revealing that Tetra III surpasses Tetra II with a total absolute rotation and center shift of 121.19° and 3.5 mm, respectively, compared to values of 94.39° and 14.36 mm observed for Tetra II. The main contributions of this article are as follows:

- Introduction of a novel design modification (Tetra III) to address joint stiffening observed in the Tetra II compliant mechanism.
- Utilization of a computer-aided engineering (CAE) framework incorporating Finite Element Analysis (FEM) to optimize the spatial compliant mechanisms.
- Development and validation of a Pseudo-Rigid-Body equivalent model to facilitate faster simulations in a multi-body environment.
- Introduction of Tetra III, a novel design characterized by higher joint mobility due to the avoidance of self-collisions and improved overall ROM compared to Tetra II.
- Comparison of the optimized Tetra III joint with the original Tetra II design in terms of ROM and center shift.

- A physical prototype of the Tetra III joint is fabricated, showcasing the feasibility of the proposed design for real-world implementation.

The remainder of this paper is organized as follows: Section 2 presents the geometric model of the Tetra III joint, which is utilized to obtain a parametric model for optimizations. In Section 3, the CAE optimization framework is discussed. Section 4 compares the novel Tetra III joint to the Tetra II joint in terms of their ROM and center shift. Section 5 presents and validates the PRB model of the optimized Tetra III joint. Section 6 demonstrates the fabrication ability of the tetra III joint through an SLS printed prototype. Finally, Section 7 concludes the research.

2 Tetra III geometric model

To properly establish the optimization procedure outlined in Section 3, it is crucial to define the key geometric parameters of the tetrahedral joint. Additionally, it's important to distinguish which parameters will serve as independent variables and which as dependent variables. To simplify the discussion in this section, we will focus on tetrahedron elements formed by isosceles triangles. In other words, referring to Fig. 3, we will assume $l_{1,1} = l_{2,1}$ and $l_{1,2} = l_{2,2}$. Specifically, the decision was made to keep the lengths of the segment $l_{1,1}$ of the external triangle and the value of the z-coordinate of the Center of Instantaneous Rotation (CIR) of the spherical joint z_{CIR} at a constant value, set to 40 mm for both. This choice is justified by the fact that the primary constraint during the design phase usually relates to spatial considerations. As independent variables, the angular value θ between the two equal segments of the isosceles triangle and the offset value Δ between the legs of the inner and outer triangles were selected. Given these four dimensions and referring to the coordinate system reported in Fig. 3, all the coordinates of the vertices can be easily obtained as follows:

$$A_1(x, y, z) = (0, 0, 0)$$

$$B_1(x, y, z) = (l_{1,1} * \cos(\frac{\theta}{2}), l_{1,1} * \sin(\frac{\theta}{2}), 0)$$

$$C_1(x, y, z) = (l_{1,1} * \cos(\frac{\theta}{2}), -l_{1,1} * \sin(\frac{\theta}{2}), 0)$$

$$A_2(x, y, z) = (\frac{\Delta}{\sin\frac{\theta}{2}}, 0, D)$$

$$B_2(x, y, z) = (\frac{\Delta}{\sin\frac{\theta}{2}} + l_{2,1} * \cos\frac{\theta}{2}, l_{2,1} * \sin\frac{\theta}{2}, D)$$

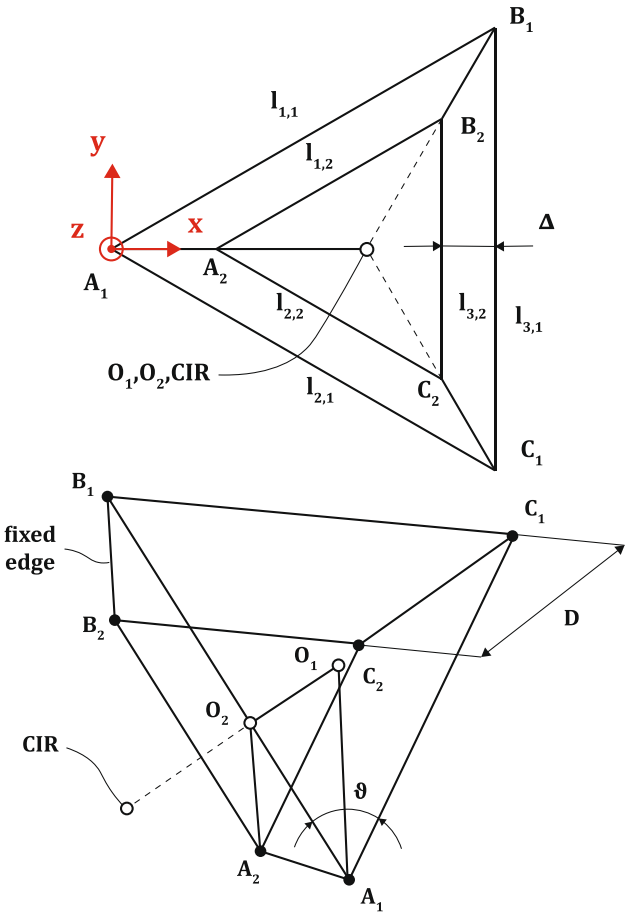

Fig. 3 TETRA III design parameters

$$C_2(x, y, z) = (\frac{\Delta}{\sin\frac{\theta}{2}} + l_{2,1} * \cos\frac{\theta}{2}, -l_{2,1} * \sin\frac{\theta}{2}, D)$$

where

$$l_{2,1} = l_{1,1} * \cos(\frac{\theta}{2}) - \Delta - \frac{\frac{\Delta}{\sin\frac{\theta}{2}}}{\cos\frac{\theta}{2}}$$

$$D = \frac{z_{CIR} * (l_{2,1} - l_{1,1})}{l_{1,1}}$$

are, respectively, the length of the equal side of the internal isosceles triangle and the thickness of the tetrahedron. Lastly, by positioning points O_1 and O_2 at the barycenters of their respective triangles and identifying the point representing the CIR of the tetrahedral joint as the intersection of two lines in space, each passing through one of the three tetrahedral edge connecting the CIR, it is possible to formulate the final equations needed for constructing the joint as:

$$O_1(x, y, z) = (\frac{2 * l_{1,1} * \cos\frac{\theta}{2}}{3}, 0, 0)$$

$$O_2(x, y, z) = (\frac{\Delta}{\sin\frac{\theta}{2}} + \frac{2 * l_{2,1} * \cos\frac{\theta}{2}}{3}, 0, D)$$

$$CIR(x, y, z) = (\frac{l_{1,1}}{l_{1,1} - l_{2,1}} * \frac{\Delta}{\sin\frac{\theta}{2}}, 0, z_{CIR})$$

By incorporating these straightforward equations into a Python script, along with the necessary commands for creating sketches and 3D blends within Spaceclaim, it becomes possible to programmatically update the geometry of the tetrahedral joint in Ansys Workbench. This streamlined approach facilitates the optimization procedure based on shell element FEM analysis in the most efficient manner. As illustrated in Fig. 3, the updated joint comprises a single outer tetrahedral shell. In this configuration, one edge (i.e., $\overline{B_1B_2}$) is fixed, while a second edge (i.e., $\overline{A_1A_2}$) is rigidly connected to the segment linking the centroids of the two triangles, $\overline{O_1O_2}$. This design minimizes the risk of self-contact during deflection, addressing a critical concern for enhanced joint performance.

3 CAE optimization framework

In this section, the optimization procedure employed to maximize the ROM of the Tetra III joint will be detailed. Figure 4 illustrates the key steps implemented within the Ansys Workbench software. For programmatic variation of the model's geometry during the optimization process, meticulous preparation of the geometry (within the corresponding block) is essential. As previously discussed in Section 3, the use of Spaceclaim software enables the creation of Python scripts capable of dynamically recreating the model based on the updated Δ and θ parameters at each optimization iteration. However, depending solely on the geometry update is inadequate, as Ansys, within the "model" block, necessitates consistent references for applying constraints and forces. These references, referred to as "named selections" within the software, include the edge designated for the "fixed" boundary condition, the edge connected to the joint's barycentric line, and the external surface of the joint. It becomes imperative to create and maintain these references through the geometry generation script to ensure their recognition and automatic update within the "model" block. This integration is crucial for the smooth execution of the optimization process.

3.1 Finite element model

Referring to Fig. 5, the model employed for the joint study is straightforward to explain. Leveraging the named selections generated by the geometry generation script, a fixed support is applied to one edge of the tetrahedral joint ($\overline{B_1B_2}$, as depicted in Fig. 3). Material properties, such as Nylon with a Young's modulus of 1400 MPa and a Poisson's ratio of 0.4, are assigned to its external surface so that it reflects the material used for the prototype. Such plastics hold promise for creating joints with substantial displacements, applicable in various fields such as aerospace, medical, and robotics [17]. The Tetra III joint was fabricated using a 3D Systems ProX SLS 6100 machine, employing Duraform as the construction material. Duraform PA, a durable polyamide 12 thermoplastic commonly known as Nylon, was selected for its excellent structural properties [34]. Moreover, this material exhibits near-isotropic behavior once manufactured, further enhancing the joint's overall performance. Notably, Duraform PA possesses a high value of deformation at break (14%), making

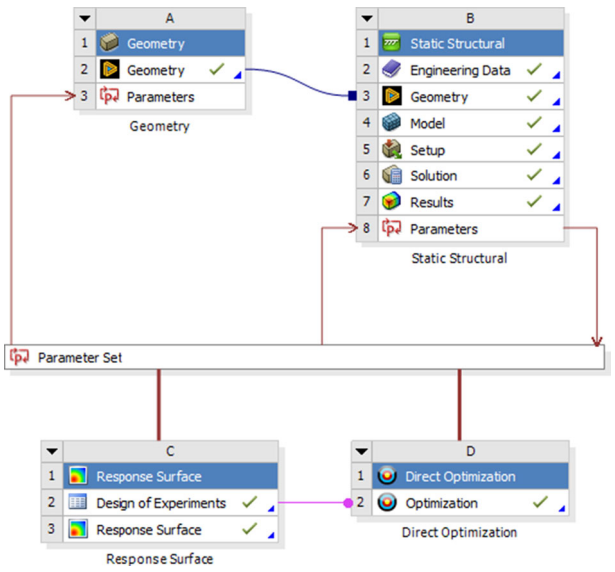

Fig. 4 Tetra III Ansys Workbench optimization steps

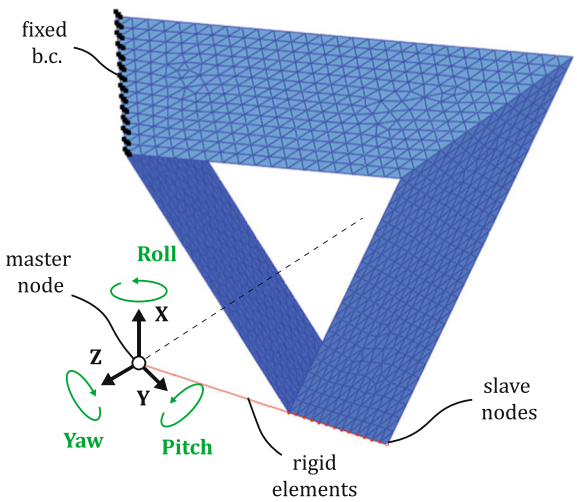

Fig. 5 Shell-based model

it particularly suitable for constructing compliant mechanisms.

Furthermore, a master node (referred to as the "remote point" in Ansys) is established at the coordinates of the CIR. This master node is rigidly connected to the nodes within the named selection of the joint's second edge ($\overline{A_1A_2}$, referencing Fig. 3). Finally, moments are applied at this remote point in the three principal directions (x, y, and z), encompassing both positive and negative orientations. This results in a total of 6 moments, as visually represented in Fig. 6.

The mesh, generated using SHELL181 elements, is comprised of 264 nodes and 212 elements, with a minimum element size set to 0.5 mm. This particular size was chosen as a balanced compromise between result precision and simulation efficiency, a crucial consideration given its integration with an optimization procedure. Notably, the "large deflection" option must be enabled in the software for reliable results. Additionally, a shell thickness of 1 mm has been specified.

The entire model, as configured, requires less than 3 minutes for resolution on an Intel(R) Core(TM) CPU @ 2.5 GHz and 16 GB RAM workstation. As a performance metric for the joint, we measure the maximum rotation angles at the master node, along with the maximum positional error at the same node during the application of couples.

3.2 Optimization problem

Referring to Fig. 4, the internal optimizer within Ansys initially employs a Design of Experiment (DOE) to identify optimal starting points for the subsequent optimization process. A Latin Hypercube-type DOE, comprising 200 points, was used. As previously mentioned, the independent variables include the angle θ and the offset value between the two triangles of the tetrahedral joint, Δ, varied within the ranges of [30°, 130°] and [4 mm, 8 mm], respectively.

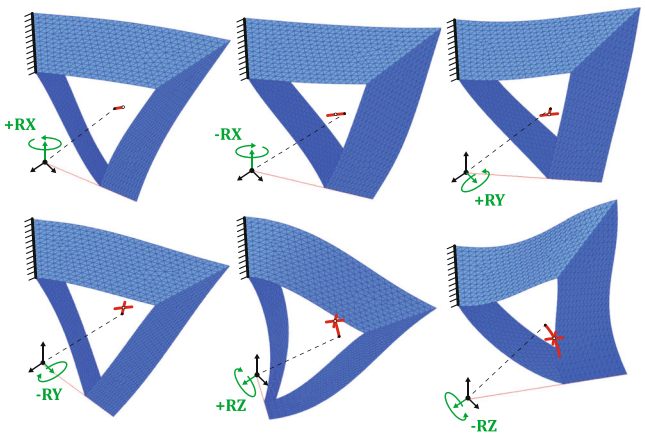

Fig. 6 TETRA III shell model under all 6 rotations

Based on the DOE results, a subsequent optimization aimed to maximize the absolute values of the 6 rotations (+RX, -RX, +RY, -RY, +RZ, -RZ), while imposing a constraint not to exceed a maximum stress of 40 MPa. This constraint is set against a maximum material yield strength of 60 MPa, reflecting a conservative estimate due to the potential concentration of stresses in the final 3D model resulting from the thickening of rigid parts during fabrication. The optimization problem can be formulated as follows:

$$
\begin{aligned}
&maximize \quad (|\pm RX|, |\pm RY|, |\pm RZ|)\\
&\text{with respect to} \quad \Xi = [\Delta, \theta]\\
&\text{subject to} \quad \sigma_{MAX} < 40MPa;\ \Xi \in [\Xi_{\min}, \Xi_{\max}]
\end{aligned}
$$

3.3 Results

The optimal values of the independent variables, along with the corresponding performance indices resulting from the optimization, are summarized in Table 1. These values underscore the remarkable ROM achieved in proportion to the compact dimensions of the component, especially along Z-direction. To conclude this section and validate the optimization performed, the final design of the Tetra joint was modeled and analyzed under conditions consistent with the shell element model. The mesh for this model comprises 45,312 nodes and 23,363 SOLID187 elements. The model is depicted in Fig. 7, and the final results obtained will be detailed in Section 4, where they will be compared with those achieved using the Tetra II joint.

4 Comparison of Tetra III and Tetra II

In the subsequent analysis, a comparative evaluation between Tetra III and Tetra II will be conducted, with a specific focus on their rotational capabilities and center shifts. The objective is to shed light on the enhanced features of the Tetra III joint, emphasizing its improved ROM and minimized cen-

Table 1 Optimal values of the Tetra III joint

Design Var.	Range	Opt. value
Independent variables		
θ	[30,130]°	104.58°
Δ	[4,8] mm	4.58 mm
Design Var.	**Max. value**	
Performance indexes		
$\pm RX$	[−2.52,+3.47] °	
$\pm RY$	[−16.06,+16.57] °	
$\pm RZ$	[−40.99,+43.22] °	

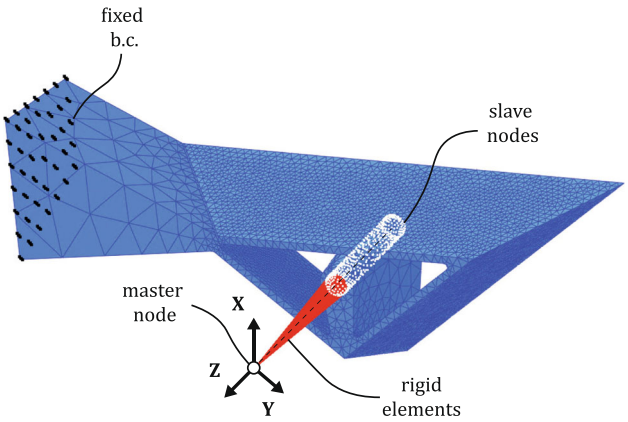

Fig. 7 Final design FEM model

ter shift resulting from the modification of the triangle type, rather than the introduction of additional layers that might complicate the structure.

The assessment involves an examination of the maximum rotations around the X, Y, and Z axes in both positive and negative directions for both Tetra II and Tetra III. Additionally, the center shifts in the remote center of rotation are evaluated when subjected to rotations around the X, Y, and Z axes. The comparative analysis unfolds in three key steps:

- Creation of a three-dimensional model for each design utilizing the commercial software PTC Creo.
- Application of rotations about the positive and negative directions of the X, Y, and Z axes to the end-effectors of each design within Ansys.
- Measurement of the maximum rotations of the end-effectors in degrees, along with the corresponding center shifts.

The maximum rotations and center shifts are measured at either the point of maximum yield strength or when they collide with their edges. Figure 8 displays the two tetras where the maximum rotations were measured. The simulation results are normalized and standardized for comparison, and are depicted in Fig. 9. These results can be summarized as follows:

- In the X-direction rotation, Tetra II achieved a maximum positive rotation of 8.64° and a maximum negative rotation of 8.62°, while Tetra III exhibited values of 6.25° and 2.61°, respectively.
- In the Y-direction rotation, Tetra II recorded a maximum positive rotation of 15.17° and a maximum negative rotation of 10.84°, whereas Tetra III demonstrated values of 13.37° and 15.24°, respectively.

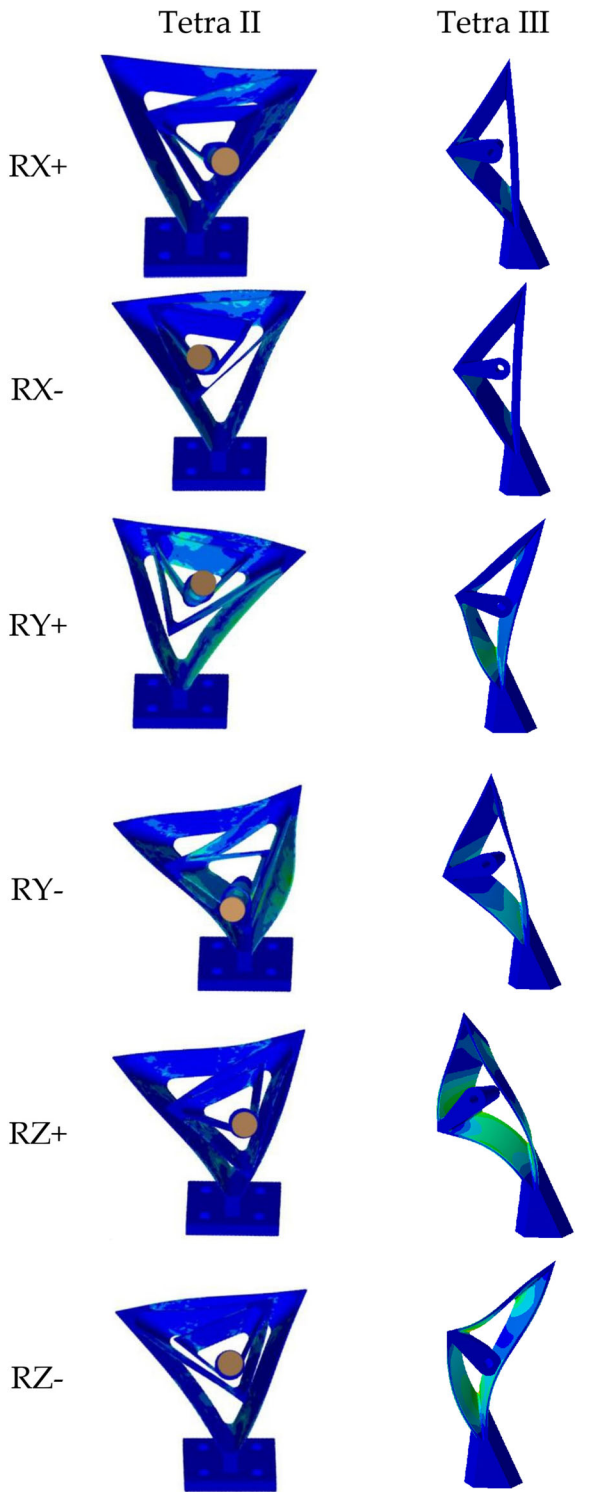

Fig. 8 Deflected joints at either the point of maximum yield strength or when they collide with their edges

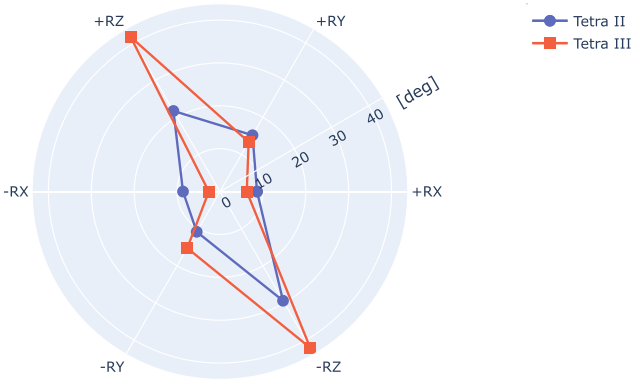

Fig. 9 Maximum ROM of Tetra II and Tetra III

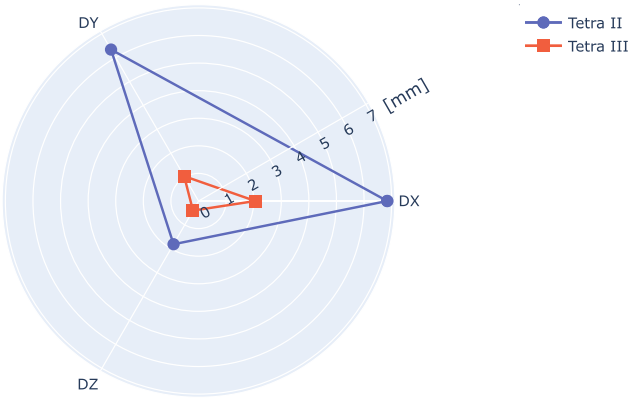

Fig. 11 Maximum center shift errors of Tetra II and Tetra III

- For rotation about the Z-direction, Tetra II attained a maximum positive rotation of 21.71° and a maximum negative rotation of 29.41°. In contrast, Tetra III showed values of 41.63° and 42.09°.

Hence, we observe that the new Tetra model achieves a notable enhancement in the ROM along the Z-direction, albeit with a slight reduction in ROM along the X-direction. Specifically, the increase along the positive Z-direction is nearly twofold. This outcome holds significance, particularly in the context of the stringent dimensional constraints imposed for the Delta robot application illustrated in Fig. 1. Figure 10 visually highlights the substantial dimensional reduction achieved with the new joint design. In conclusion, the maximum observed center shift values for both joints are presented in Fig. 11. Surprisingly, these values are considerably lower than those observed for the Tetra II joint, despite the optimization solely targeting the ROM of the component. This noteworthy outcome suggests that the absence of internal layers within the component contributes to an augmentation in both the ROM and the precision of the spherical joint.

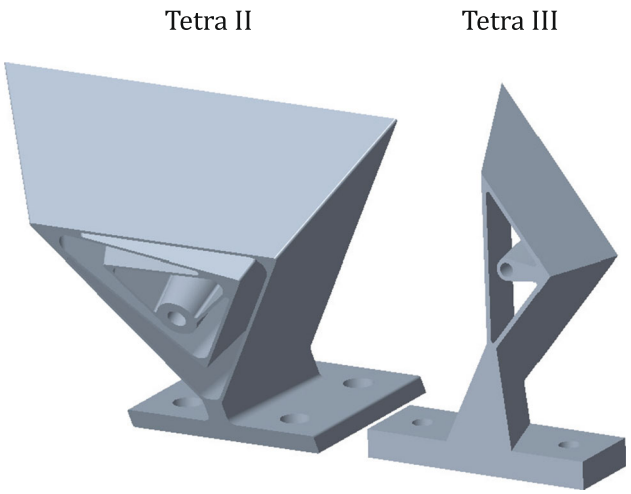

Fig. 10 Dimensional comparison of Tetra II and Tetra III

5 PRB modelling

Compliant mechanisms have gained widespread use in diverse engineering applications due to their ability to achieve high precision with a reduced number of components. The PRB method is a common approach employed in the analysis and design of compliant mechanisms. This method models the behavior of flexible elements by representing them as interconnected rigid links, utilizing spring-loaded kinematic pairs like spherical, prismatic, or revolute joints. The adoption of the PRB technique provides engineers with notable advantages. Firstly, it enhances computational efficiency in simulating compliant mechanisms, surpassing traditional Finite Element Method (FEM) approaches. Secondly, it allows for the utilization of well-established methods and software tools, including specialized Multibody Dynamics (MBD) environments tailored for analyzing rigid-link mechanisms.

However, it is crucial to recognize the inherent limitations of the PRB method, requiring a case-by-case assessment. These limitations include the potential dependency of PRB parameters on applied loads when inadequate mobility exists within the chosen PRB topology. Additionally, the PRB method may not precisely capture nonlinear effects during significant deflections, such as material nonlinearity, geometric nonlinearity, and load-stiffening phenomena. To ensure reliability, compliant mechanism architectures designed using the PRB method are typically validated at the end of the design process through alternative techniques, such as FEM simulations or experimental testing [1].

The pseudo-rigid equivalent model of the Tetra III joint was constructed following the model of folded leaf springs, as detailed in [5]. This model, shown in Fig. 12, incorporates

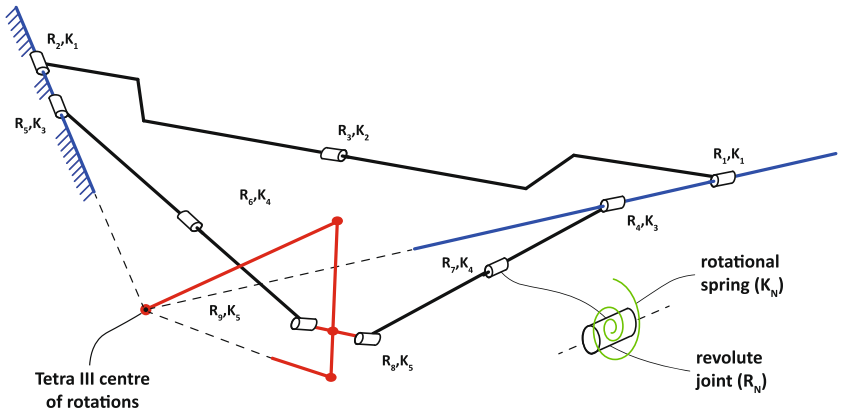

Fig. 12 Pseudo-Rigid TETRA III equivalent model

a total of 9 revolute joints and rotational springs. Due to the symmetry of the component, only 5 of these rotational springs are unique. The K_N values in the model serve as unknowns to be determined based on FEM results.

To determine these values, internal optimization was conducted within the RecurDyn multi-body environment through the AUTODESIGN toolkit. This toolkit utilizes a Latin-Hypercube Design of Experiment to deliver enhanced solutions for parameter estimation problems in a time-effective manner. The optimization aimed to minimize the angular position error of the joint, sequentially subjected to the 6 torques illustrated in Fig. 6. Optimizing the values with respect to all 6 loads allowed the development of a PRB model with a higher overall error but greater versatility than could be achieved by individually applying each load. In fact, the PRB model technique exhibits high sensitivity to changes in applied loads, making it challenging to obtain optimal stiffness values identical for every applied loadset.

In this scenario, the objective function F_{err} to be minimized is defined as the discrepancy between the absolute of the angular values along the X, Y, and Z axes measured at the end-effector of the PRB model and those obtained from the previous FEM analysis:

$$F_{err} = a * |RX_{PRB} - RX_{FEM}| + b * |RY_{PRB} - RY_{FEM}| + c * |RZ_{PRB} - RZ_{FEM}|$$

where a, b, and c are coefficients used to normalize the weight of the three errors concerning the maximum values measured by the FEM for the RX, RY, and RZ angles. Specifically, using c as the normalization value for the three errors, we obtain $a = 6.73$, $b = 2.76$ and $c = 1$.

In Fig. 13, the results obtained after optimizing the PRB model are presented, revealing its inherent limitations. Notably, when examining rotation around the Z-axis, the model deviates from the FEM as the rotation exceeds a certain threshold. However, it demonstrates relatively accurate performance for more moderate rotations, particularly when considering all six rotations simultaneously, a scenario that challenges the model. The resolution time for this model is approximately 0.2 seconds, a fraction of the time required for the corresponding FEM using the same workstation, making it a competitive option for multi-body simulations involving numerous joints.

6 Fabrication

The fabricationability of the Tetra III joint showcases its versatility and adaptability in the manufacturing process. Here, we employed selective laser sintering (SLS) as the chosen manufacturing technology due to its cost-effectiveness and the absence of support structure requirements. This approach allowed for efficient fabrication of the joint. Additionally,

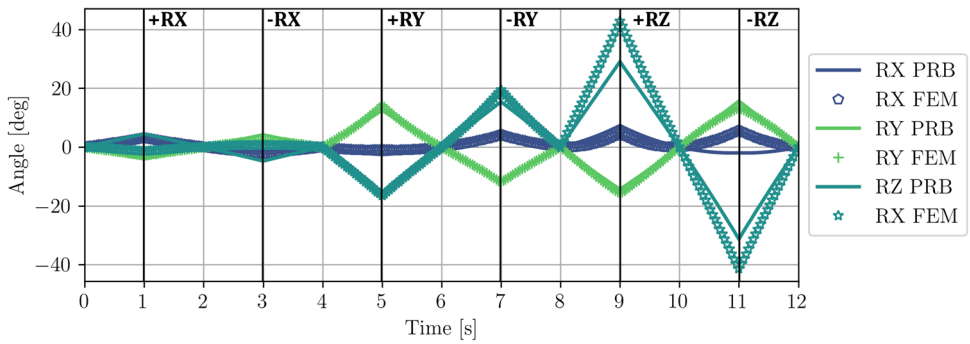

Fig. 13 TETRA III, comparison between PRB model and FEM model

our implementation of the Design for Additive Manufacturing (DfAM) methodology resulted in a geometric design that is well-suited for fused filament fabrication (FFF) printers, which are widely available. The Tetra III joint was fabricated using a 3D Systems ProX SLS 6100 machine, utilizing Duraform as the construction material. Duraform PA, a durable polyamide 12 thermoplastic commonly known as Nylon, was selected for its excellent structural properties. Moreover, this material exhibits near-isotropic behavior once manufactured, further enhancing the joint's overall performance. Notably, Duraform PA possesses a high value of deformation at break (14%), making it particularly suitable for constructing compliant mechanisms. By leveraging the advantages of selective laser sintering and the adaptability of fused filament fabrication printers, the fabrication process of the Tetra III joint demonstrates its feasibility, while the use of Duraform PA as the construction material and the optimized flexure design contribute to its robustness and compliance.

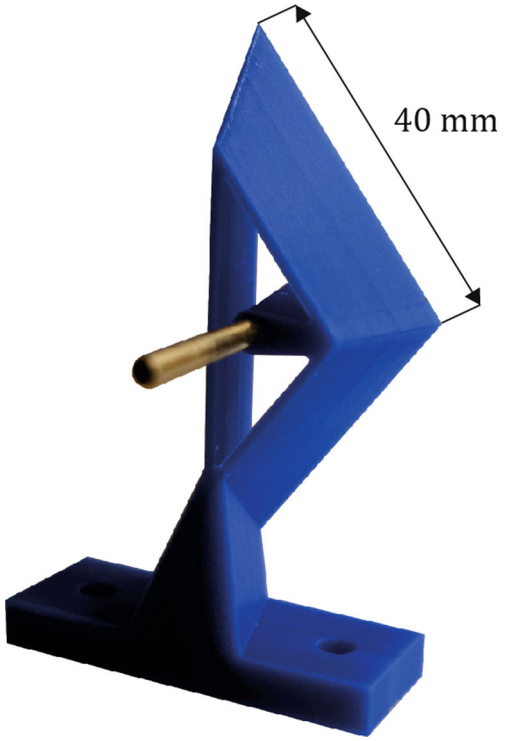

Fig. 14 Prototype of the Tetra III

7 Conclusions

This study delved into optimizing a novel spherical compliant joint derived from the Tetra II joint, aiming to enhance the ROM in the context of a Delta robot design. Leveraging a comprehensive CAE framework that integrates Spaceclaim and Ansys Workbench, the Tetra II joint configuration underwent optimization to maximize its rotational capabilities. The research also explored the development of a rigid-equivalent model using the PRBM technique, enabling swift simulations in a multi-body environment.

The results indicated that the Tetra III design, characterized by a more obtuse triangle in comparison to the previous iteration, exhibited increased overall rotations (121.19° versus 94.39°) and reduced overall center shift (3.5 mm versus 14.36 mm) compared to Tetra II. This underscores the effectiveness of the optimization strategy and emphasizes the substantial impact of the triangle type on the joint's performance. In the final phase, the Tetra III joint was fabricated to illustrate its manufacturability. Using selective laser sintering (SLS) technology and Duraform PA as the construction material, the joint was successfully and efficiently manufactured (Fig. 14).

Future research could explore how material selection affects stiffness and stress distribution in achieving desired performance. Investigating the impact of various materials, including advanced options, on the joint's overall performance within its intended application is crucial. Future research should delve into studying the fatigue response and operational lifetime of Tetra joints. Additionally, exploring scalability and adaptation for different sizes or load requirements is crucial and requires attention in subsequent research.

Author Contributions Conceptualization: all authors contributed to the study conception. Methodology: SMK, AP, MB, and GB. Software: SMK and MB. Validation: SMK and MB. Prototyping: EO and AP. Writing — original draft preparation: SMK, AP, MB and GB. Writing — review and editing: AP, MB, EO, GB, and GH. Visualization: SMK. Supervision: GB, GH, and AP. All authors read and approved the final version of the manuscript.

Funding Open access funding provided by Università degli Studi di Genova within the CRUI-CARE Agreement. This research was conducted as part of the Horizon Europe Program through the INTELLIMAN project (https://intelliman-project.eu/). The INTELLIMAN Project is funded by the European Union under grant agreement ID: 101070136.

Data Availability CAD and FEM models will be made available after paper acceptance.

Code availability Not applicable.

Declarations

Ethics approval Not applicable.

Consent to participate Not applicable.

Consent for publication Not applicable.

Competing interests The authors declare no competing interests.

References

1. Bilancia P, Berselli G, Bruzzone L, Fanghella P (2019) A cad/cae integration framework for analyzing and designing spatial compliant mechanisms via pseudo-rigid-body methods. Robot Computer-Integrated Manufac 56:287–302
2. Howell LL (2013) Compliant mechanisms. In: 21st Century Kinematics: The 2012 NSF Workshop, Springer, pp 189–216
3. Tadesse Y, Wu L, Saharan LK (2016) Musculoskeletal system for bio-inspired robotic systems. Mech Eng 138(03):S11–S16
4. Ikemoto S, Kimoto Y, Hosoda K (2015) Shoulder complex linkage mechanism for humanlike musculoskeletal robot arms. Bioinspiration Biomimet 10(6):066009
5. Rommers J, van der Wijk V, Herder JL (2021) A new type of spherical flexure joint based on tetrahedron elements. Precision Eng 71:130–140
6. Baggetta M, Palli G, Melchiorri C, Berselli G A monolith cable-driven compliant wrist for prosthetic arms. IEEE/ASME Trans Mechatron
7. Hao G, He X, Zhu J, Li H (2024) Design and Analysis of Leaf Beam Single-Translation Constraint Compliant Modules and the Resulting Spherical Joints. J Mech Design 01:1–15
8. Moon Y-M, Kota S (2002) Design of compliant parallel kinematic machines. In: International design engineering technical conferences and computers and information in engineering conference, Vol. 36533, American Society of Mechanical Engineers, pp 35–41
9. Wu T-L, Chen J-H, Chang S-H (2008) A six-dof prismatic-spherical-spherical parallel compliant nanopositioner. IEEE Trans Ultrasonics, Ferroelectrics, Frequency Control 55(12):2544–2551
10. Brecher C, Pyschny N, Behrens J (2010) Flexure-based 6-axis alignment module for automated laser assembly. In: Precision assembly technologies and systems: 5th IFIP WG 5.5 International Precision Assembly Seminar, IPAS 2010, Chamonix, France, February 14-17, 2010. Proceedings 5, Springer, pp 159–166
11. Dong W, Sun L, Du Z (2008) Stiffness research on a high-precision, large-workspace parallel mechanism with compliant joints. Precision Eng 32(3):222–231
12. Howell LL, Magleby SP, Olsen BM Handbook of compliant mechanisms
13. Naves M, Aarts R, Brouwer D (2019) Large stroke high off-axis stiffness three degree of freedom spherical flexure joint. Precision Eng 56:422–431
14. Lobontiu N, Paine JS (2002) Design of circular cross-section corner-filleted flexure hinges for three-dimensional compliant mechanisms. J Mech Des 124(3):479–484
15. Soemers HM (2010) Design principles for precision mechanisms
16. Trease BP, Moon Y-M, Kota S (2005) Design of large-displacement compliant joints. J Mech Des 127(3):788–98
17. Parmiggiani A, Ottonello E, Masoud Kargar S, Baggetta M, Hao G, Berselli G (2023) Deltaflex: An additively manufactured monolithic delta robot with compliant joints. In: International design engineering technical conferences and computers and information in engineering conference, Vol. 87363, American Society of Mechanical Engineers, pp V008T08A031
18. Do TV, Nam NQ, Vinh DD, Viet NQ, Dat PN, Van Hung T (2021) Design of delta robot using image processing for product sorting process. In: 2021 International conference on system science and engineering (ICSSE), IEEE, pp 210–214
19. Xiao B, Alamdar A, Song K, Ebrahimi A, Gehlbach P, Taylor RH, Iordachita I (2022) Delta robot kinematic calibration for precise robot-assisted retinal surgery. In: 2022 International symposium on medical robotics (ISMR), IEEE, pp 1–7
20. Nedic N, Prsic D, Dubonjic L, Stojanovic V, Djordjevic V (2014) Optimal cascade hydraulic control for a parallel robot platform by pso. Int J Adv Manufac Technol 72:1085–1098
21. Bruyas A, Geiskopf F, Meylheuc L, Renaud P (2014) Combining multi-material rapid prototyping and pseudo-rigid body modeling for a new compliant mechanism. In: 2014 IEEE International conference on robotics and automation (ICRA), IEEE, pp 3390–3396
22. A Neutrally Stable Quasi-Compliant Spherical Joint With a Remote Center of Rotation, Vol. Volume 7: 46th Mechanisms and Robotics Conference (MR) of International Design Engineering Technical Conferences and Computers and Information in Engineering Conference (2022)
23. Wiersma DH, Boer SE, Aarts RGKM, Brouwer DM (2013) Design and Performance Optimization of Large Stroke Spatial Flexures. J Comput Nonlinear Dynamics 9(1):11
24. Naves M, Brouwer DM, Aarts RGKM (2017) Building Block-Based Spatial Topology Synthesis Method for Large-Stroke Flexure Hinges. J Mech Robot 9(4):05
25. Bilancia P, Berselli G, Bruzzone L, Fanghella P (2017) A practical method for determining the pseudo-rigid-body parameters of spatial compliant mechanisms via cae tools. Procedia Manufacturing, 11:1709–1717. In: 27th International Conference on Flexible Automation and Intelligent Manufacturing, FAIM2017, 27-30 June 2017, Modena, Italy
26. Ottonello E, Baggetta M, Berselli G, Parmiggiani A (2023) Design and validation of a push-latch gripper made in additive manufacturing. IEEE/ASME Trans Mechatron 1–9
27. Bilancia P, Berselli G (2021) An overview of procedures and tools for designing nonstandard beam-based compliant mechanisms. CAD Computer Aided Design, 134. Cited by: 30
28. Kuo C-C, Gurumurthy N, Chen H-W, Hunag S-H (2023) Experimentation and numerical modeling of peak temperature in the weld joint during rotary friction welding of dissimilar plastic rods. Polymers 15(9)
29. Kuo C-C, Tasi Q-Z, Hunag S-H (2022) Development of an epoxy-based rapid tool with low vulcanization energy consumption channels for liquid silicone rubber injection molding. Polymers 14(21)
30. Wang B-W, Nian S-C, Huang M-S (2022) Strategies for adjusting process parameters in cae simulation to meet real injection molding condition of screw positions and cavity pressure curves. Int J Adv Manufac Technol 122:08
31. Ma Y, Dang K, Wang X, Zhou Y, Yang W, Xie P (2023) Intelligent recommendation system of injection molding process parameters based on cae simulation, process window and machine learning
32. Yamashita Y, Uematsu H, Tanoue S (2023) Calculation of strain energy density function using ogden model and mooney rivlin model based on biaxial elongation experiments of silicone rubber. Polymers 15(10)

33. Ktari A, El Mansori M (2023) On the improvement of castings quality in hybrid low-pressure sand-casting (lpsc) process in a fully integrated cae environment. Int J Adv Manufac Technol 127(06):1–18

34. Rybansky D, Marsalek P, Sotola M, Hroncek J, Drahorad L, Kusnir O, Prokop J (2023) Design and behavior of lightweight flexible structure with spatial pattern reducing contact surface fraction. Polymers 15(19)

Authors and Affiliations

Seyyed Masoud Kargar[1] · Alberto Parmiggiani[2] · Mario Baggetta[1] · Emilio Ottonello[2,3] · Guangbo Hao[4] · Giovanni Berselli[1,5]

Seyyed Masoud Kargar
seyyed.masoud.kargar@edu.unige.it

Alberto Parmiggiani
alberto.parmiggiani@iit.it

Mario Baggetta
mario.baggetta@unige.it

Emilio Ottonello
emilio.ottonello@iit.it

Guangbo Hao
g.hao@ucc.ie

[1] Department of Mechanical, Energy, Management and Transportation Engineering (DIME), University of Genova, Genoa, Italy

[2] Mechanical Design and Manufacturing Facility, Centre for Robotics and Intelligent Systems (CRIS), Fondazione Istituto Italiano di Tecnologia (IIT), Genoa, Italy

[3] Department of Informatics, Bioengineering, Robotics and Systems Engineering (DIBRIS), University of Genova, Genoa, Italy

[4] School of Engineering and Architecture-Electrical and Electronic Engineering, University College Cork, Cork, Ireland

[5] Advanced Robotics Department (ADVR), Fondazione Istituto Italiano di Tecnologia (IIT), Genoa, Italy